Nano-Micro Letters

ISSN 2311-6706
e-ISSN 2150-5551
CN 31-2103/TB

ARTICLE

https://doi.org/10.1007/s40820-020-0392-8

Cite as
Nano-Micro Lett.
(2020) 12:61

Received: 2 December 2019
Accepted: 12 January 2020

$NiSe_2/Ni(OH)_2$ Heterojunction Composite through Epitaxial-like Strategy as High-Rate Battery-Type Electrode Material

Hao Mei[1], Zhaodi Huang[1], Ben Xu[1,2,3] ✉, Zhenyu Xiao[4], Yingjie Mei[2], Haobing Zhang[1], Shiyu Zhang[1], Dacheng Li[5], Wenpei Kang[1], Dao Feng Sun[1,2] ✉

Hao Mei and Zhaodi Huang have contributed equally to this work

✉ Ben Xu, benxu@upc.edu.cn; Dao Feng Sun, dfsun@upc.edu.cn

[1] College of Science, China University of Petroleum (East China), Qingdao 266580, Shandong, People's Republic of China

[2] School of Material Science and Engineering, China University of Petroleum (East China), Qingdao 266580, Shandong, People's Republic of China

[3] Key Laboratory of Structural Chemistry, Fujian Institute of Research on the Structure of Matter, Chinese Academy of Sciences, Fuzhou 350002, People's Republic of China

[4] Key Laboratory of Eco-chemical Engineering, Ministry of Education Laboratory of Inorganic Synthesis and Applied Chemistry, College of Chemistry and Molecular Engineering, Qingdao University of Science and Technology, Qingdao 266402, Shandong, People's Republic of China

[5] Shandong Provincial Key Laboratory of Chemical Energy Storage and Novel Cell Technology, School of Chemistry and Chemical Engineering, Liaocheng University, Liaocheng 252059, Shandong, People's Republic of China

HIGHLIGHTS

- A facile and effective epitaxial-like growth strategy is applied to fabricate the $NiSe_2/Ni(OH)_2$ heterojunction composite.
- The assembled asymmetric supercapacitor based on the heterojunction composite surpasses most of the reported results. It is the first time that the powdered electrode materials can have such large capacity, high rate, and extreme long cycle life.

ABSTRACT Constructing heterojunction is a promising way to improve the charge transfer efficiency and can thus promote the electrochemical properties. Herein, a facile and effective epitaxial-like growth strategy is applied to $NiSe_2$ nano-octahedra to fabricate the $NiSe_2$-(100)/$Ni(OH)_2$-(110) heterojunction. The heterojunction composite and $Ni(OH)_2$ (performing high electrochemical activity) is ideal high-rate battery-type supercapacitor electrode. The $NiSe_2/Ni(OH)_2$ electrode exhibits a high specific capacity of 909 C g^{-1} at 1 A g^{-1} and 597 C g^{-1} at 20 A g^{-1}. The assembled asymmetric supercapacitor composed of the $NiSe_2/Ni(OH)_2$ cathode and p-phenylenediamine-functional reduced graphene oxide anode achieves an ultrahigh specific capacity of 303 C g^{-1} at 1 A g^{-1} and a superior energy density of 76.1 Wh kg^{-1} at 906 W kg^{-1}, as well as an outstanding cycling stability of 82% retention for 8000 cycles at 10 A g^{-1}. To the best of our knowledge, this is the first example of $NiSe_2/Ni(OH)_2$ heterojunction exhibiting such remarkable supercapacitor performance. This work not only provides a promising candidate for next-generation energy storage device but also offers a possible universal strategy to fabricate metal selenides/metal hydroxides heterojunctions.

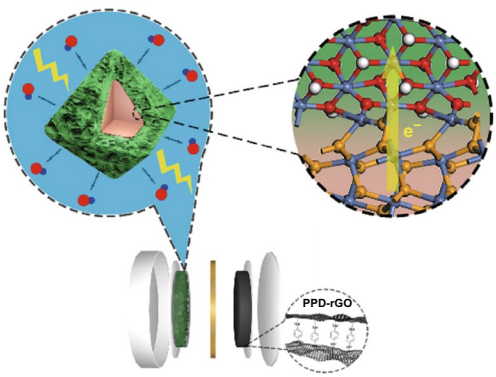

KEYWORDS Supercapacitor; Heterojunction; Epitaxial-like growth; $NiSe_2/Ni(OH)_2$

Published online: 21 February 2020

1 Introduction

Due to the severe consumption of fossil energy and environmental issues, it is urgent to develop novel clean-energy technologies, including solar, wind, and tide [1]. After harvesting, these energy usually cannot directly parallel to the grids due to their severe fluctuations, thus energy storage devices affording large charging/discharging currents and long cycle lives are urgently needed [2–5]. Scientists have paid much efforts to develop energy storage devices, such as lithium/sodium/potassium ion batteries, fuel cells, and electrochemical supercapacitors [6–10]. Among them, supercapacitors are attractive due to their high safety, long cycle lives, large power densities, and low cost [11–13]. However, their low energy densities, compared with other electrochemical energy technologies, limit their further applications [14–16]. Several methods have been utilized to improve the energy storage performance of supercapacitor, and fabricating asymmetric supercapacitor is believed to be an ideal solution [17–19]. An asymmetric supercapacitor is composed of an electric double-layer capacitive (EDLC) electrode, enabling the fast energy delivery, and a pseudo-capacitive/battery-type electrode, ensuring large energy storage [20–22]. Therefore, an asymmetric supercapacitor can inherit both the advantages of large power densities from EDLC and large energy densities from pseudo-capacitive/battery-type electrode [23].

Ideal electrode material for high-performance supercapacitor should have the following features: (1) high capacity; (2) excellent rate capability; (3) long cycle lives [24]. $Ni(OH)_2$ is one of the most attractive materials due to its large theoretical capacity, easy-synthesis, and environmental friendly [25–27]. However, it still suffers from the low conductivity, which is harmful to the rate performance [28]. Furthermore, the large volume expansion during charging/discharging process leads to cycling issues [29–31]. One promising strategy to improve its supercapacitor performance is compositing $Ni(OH)_2$ with other materials. Generally, the $Ni(OH)_2$-based composite materials should have the following features. First, a considerable electron conductivity is required to compensate the low conductivity of $Ni(OH)_2$ for improving the rate capability [31]. Second, a high mechanical stability is necessary for the cycling performance [32]. Moreover, the electron transfer between different phases should be fast and efficient [33]. However, it is difficult to satisfy all the features. For instance, the most widely reported $Ni(OH)_2$/carbon composite materials have good conductivity and mechanical strength [34–36]. But the van de Waals interaction between $Ni(OH)_2$ and carbon largely limits the electron transfer efficiency between them. Recently, the composite of $Ni(OH)_2$ and Ni oxides/sulfides/phosphides was investigated as promising electrode materials, and the heterojunction structures between $Ni(OH)_2$ and Ni oxides/sulfides/phosphides are an important reason contributing to their remarkable supercapacitance behaviors [37–39]. However, there are still two issues needed to be addressed. Ni oxides/sulfides/phosphides do not perform good conductivity, much lower than carbon-based materials. Furthermore, oxidation/sulfofication/phosphorization treatments on porous $Ni(OH)_2$ are the commonly used methods, and the cycling issue is not addressed due to the relatively fragile porous $Ni(OH)_2$ basis [37]. Therefore, it is urgent to find a proper material and a proper synthesis route to obtain desired $Ni(OH)_2$-based composite materials for supercapacitor applications.

$NiSe_2$ is one semiconductor with the low resistivity below $10^{-3}\ \Omega\ cm^{-1}$ [39]. Using proper synthesis routes, $NiSe_2$ single-crystal nano-octahedra can be easily obtained and are expected to perform good conductivity with high mechanical strength due to its single-crystal feature. If porous $Ni(OH)_2$ can be properly composited to the $NiSe_2$ nano-octahedra, an ideal electrode material can be obtained, although there is no research reporting such composite as far as we know. Herein, we report an novel epitaxial-like growth strategy on the fabrication of $NiSe_2/Ni(OH)_2$ composite materials with $NiSe_2$ nano-octahedra as the precursor. Through the treatment process, Ni atoms at the surfaces of $NiSe_2$ nano-octahedra are released to the solution and coordinated to OH^- ions. And those OH^- ions simultaneously bond to the unreleased surface Ni atoms, then a close $NiSe_2/Ni(OH)_2$ heterojunction can be formed in an epitaxial-like crystallization route. Under proper reaction conditions, the obtained $NiSe_2/Ni(OH)_2$ electrode material exhibits the following advantages: (1) the heterojunction can improve electron transfer by DFT calculations; (2) large specific surface areas and suitable microporous structure ensure the abundant electrochemical active sites which are easily accessed by the electrolyte and rapid ion migration within the electrode; (3) the highly crystallized $NiSe_2$ nano-octahedra foundations provide high mechanical strength, thus the good cycling stability was obtained. As a result, the $NiSe_2/Ni(OH)_2$ electrode

https://doi.org/10.1007/s40820-020-0392-8

material obtained under optimized conditions displays the outstanding electrochemical performances of high specific capacity of 909 C g^{-1} and good cycling stability of 85% capacity retention after 5000 cycles. The asymmetric supercapacitor composed of $NiSe_2/Ni(OH)_2$ cathode and p-phenylenediamine-functional reduced graphene oxide (PPD-rGO) anode exhibits ultrahigh specific capacity of 303 C g^{-1} and remarkable energy density of 76.1 Wh kg^{-1} at the power density of 906 W kg^{-1}, as well as the excellent cycling stability of 82% capacity retention after 8000 cycles, demonstrating it a promising supercapacitor device.

2 Experiment Section

2.1 Materials Preparation

2.1.1 Preparation of $NiSe_2$ Precursor

All the chemical regents are directly used without any further purification. In a typical procedure, 0.5 mmol nickel nitrate and 3 mmol selenium powder were dissolved in 10 mL deionized water and 10 mL hydrazine hydrate solution, respectively, and mixed together. Then, the mixed solution was stirred for 30 min to obtain the clear solution. The solution was sealed in a 50 mL Teflon-lined stainless container and maintained 140 °C for 24 h. After that, the precipitation was collected by filtration, washed by deionized water and ethanol for several times, and dried at 60 °C for 24 h. Finally, the $NiSe_2$ precursor was obtained.

2.1.2 Preparation of $NiSe_2/Ni(OH)_2$

In our experiment, 0.1 g $NiSe_2$ precursor was dispersed into 20 mL 0.1 M KOH to obtain the homogeneous solution. Then, 1 mL 30% H_2O_2 was added into the solution. The mixture solution was sealed in a 50 mL Teflon-lined stainless container and maintained 170 °C for different times. The reaction product was collected by filtration, washed by deionized water and ethanol for several times, and dried at 60 °C for 24 h. For convenience, for products at different reaction times, the $NiSe_2/Ni(OH)_2$ composite was termed as $NiSe_2/Ni(OH)_2$-1h, $NiSe_2/Ni(OH)_2$-2h, $NiSe_2/Ni(OH)_2$-3h, and $NiSe_2/Ni(OH)_2$-6h, respectively. For comparison, 80 mg $NiSe_2$ precursor and 20 mg $Ni(OH)_2$ (Acros, for analysis) were physically mixed to obtain the $NiSe_2/Ni(OH)_2$ and termed as $NiSe_2/Ni(OH)_2$-Grind.

2.1.3 Preparation of PPD-rGO

The preparation of PPD-rGO is based on the previous reported works [40]. 50 mg GO was dispersed in 50 mL deionized water to form a homogeneous solution. Then, 54 mg p-phenylenediamine was added into the solution and stirred for 30 min. The mixed solution was sealed into autoclave at 180 °C for 12 h. The obtained products were washed by deionized water for several times.

2.2 Materials Characterization

Powder X-ray diffraction (XRD) was used to investigate the phase purity and crystallinity of prepared samples (Cu $K\alpha = 0.15418$ nm). X-ray photoelectron spectroscopy (XPS) was employed to examine the surface chemical states. The morphology and microstructure were examined by scanning electron microscopy (SEM) and transmission electron microscopy (TEM). Thermogravimetric analysis (TGA) tests were performed on a Mettler Toledo TGA instrument under O_2 condition at a heating rate of 10 °C min^{-1}. The N_2 adsorption/desorption curves and pore size distributions were collected from surface area analyzer ASAP-2020.

2.3 DFT Calculations

DFT calculations were performed using CASTEP in Material Studio software package [41–43]. The $Ni(OH)_2$ (110) plane was cleaved and placed on the $NiSe_2$ (100) plane. Six layers of $Ni(OH)_2$ (110) planes and three layers of $NiSe_2$ (100) planes were used, and a vacuum slab of 10 Å was added at each side to build the $NiSe_2(100)/Ni(OH)_2(110)$ heterojunction structure. The exchange–correlation functional of GGA + PBESOL is utilized for optimizing the constructed model and DOS calculations. The cutoff energy of 780 eV was used, and the norm conserving pseudopotentials were used for each type of atom. Due to the existence of Ni atoms, spin polarization was considered. FFT grid of $48 \times 48 \times 48$ and SCF tolerance of 1×10^{-5} eV/cell was used. This set is adequate for our calculations.

2.4 Electrochemical Measurements

All the electrochemical performances were tested by CHI 760e instrument. In our experiment, we used a Ni foam as current collector, platinum gage as counter electrode, 6 M KOH as electrolyte solution. For working electrode, 16 mg activated materials, 2 mg conductive carbon black, and 40 μL 5% polytetrafluoroethylene (mass radio, 8:1:1) were mixed together to get a homogenous slurry. Then, 2.5 mg of the mixture was painted on the Ni foam. Electrochemical impedance spectroscopy (EIS) was tested by using a disturbance voltage in a frequency range of 0.01–10^6 Hz. In our work, the button asymmetric supercapacitor was assembled through using 2.5 mg $NiSe_2/Ni(OH)_2$-2h of as the anode, 4 mg PPD-rGO as the cathode.

3 Results and Discussion

3.1 Mechanisms of Epitaxial-like Growth of $NiSe_2/Ni(OH)_2$ on $NiSe_2$ Nano-octahedra

The overall synthetic process of $NiSe_2/Ni(OH)_2$ heterojunction composite is shown in Fig. 1a. Initially, using nickel nitrate and selenium powder, $NiSe_2$ nano-octahedra were successfully prepared through a simple and controllable hydrothermal synthesis route. Subsequently, under the oxidative and alkaline conditions, $NiSe_2$ nano-octahedra were converted to $NiSe_2/Ni(OH)_2$ composite. As shown in Fig. 1b, c, $NiSe_2$ precursor exhibits a distinct octahedral feature in a size of 100–200 nm, and no other impurities were found. Figure 1c shows the TEM image of $NiSe_2$ octahedra, which well-matches the SEM image. The surface morphology and structure of $NiSe_2$ nano-octahedra have distinctly changed after the oxidation–hydrolysis treatment as displayed in Figs. 1d, e and S1. It is clear that the outer of $NiSe_2$ nano-octahedra is modified and surrounded by thin nanoflakes. The selected electron diffraction patterns were further employed to verify the constituent (Fig. S1). The inner and outer of nano-octahedra display the bright spots and rings feature, respectively, which illustrate that epitaxial-like growth of polycrystalline $Ni(OH)_2$ nanoflakes on the surfaces of monocrystalline $NiSe_2$ nano-octahedra.

For revealing the transformation of the $NiSe_2/Ni(OH)_2$ composites, we investigate the morphology changes of $NiSe_2/Ni(OH)_2$ composites at different reaction time, and the results are shown in Fig. 1f_1–f_4. When the reaction time reaches 1 h, a small amount of nanoflakes appear on the surfaces of nano-octahedra (Fig. 1f_1). At 2 h, the corners of nano-octahedra are corroded and a large amount of ultrathin $Ni(OH)_2$ nanoflakes crystallize and spread on the surfaces (Fig. 1f_2). However, $NiSe_2/Ni(OH)_2$-2h still presents the octahedral shape. The EDS mapping shown in Fig. 1g_1–g_4 demonstrates that the inner octahedra of $NiSe_2/Ni(OH)_2$-2h are still $NiSe_2$, consistent with the selected electron diffraction patterns, while the oxygen is well spread at the outer. When the reaction time reaches 3 h, it is clear that the octahedral block has been severely corroded and a quite number of thick nanosheets are formed (Fig. 1f_3). After 6 h of reaction time, $NiSe_2$ nano-octahedra have been almost completely destroyed, and a large amount of thick nanosheets constructed into the octahedral shape (Fig. 1f_4).

The epitaxial-like growth of the $Ni(OH)_2$ nanoflakes at the surfaces of the $NiSe_2$ nano-octahedras contributes to the heterojunction structure of $NiSe_2/Ni(OH)_2$, as demonstrated in the HRTEM images (Fig. 2). The $Ni(OH)_2$ and $NiSe_2$ domains can be clearly observed. Figure 2a is the zoom-in $Ni(OH)_2$ domain, and the hexagonal spots in the FFT image (the inset at the up-right corner) indicate that the $Ni(OH)_2$ domain is top-view of the (001) plane (the inset as the bottom-right corner). The zoom-in $NiSe_2$ domain shown in Fig. S2 is the top-view of the (001) plane due to the square spots, although slight distortion can be noticed. The measured lattice fringes at $Ni(OH)_2$ and $NiSe_2$ domains are ascribed to the $Ni(OH)_2$ (110) planes and the $NiSe_2$ (400) planes, and the distances are 1.57 and 1.49 Å, respectively (Fig. 2d, e). The epitaxial-like crystallization of $Ni(OH)_2$ on the $NiSe_2$ requires the similar lattice constant between them. As shown in Fig. S1, the (110) plane of $Ni(OH)_2$ is composed of the Ni–O octahedral layer with the distance between two Ni atoms equaling to 5.39 Å, nearly twice of the distance between two Ni atoms on the $NiSe_2$ (001) plane, it is likely that the epitaxial-like growth of $Ni(OH)_2$ on $NiSe_2$ contributing to the $NiSe_2$-(100)/$Ni(OH)_2$-(110) heterojunction.

The heterojunction can effectively facilitate the electron transportation at the interfaces. DFT calculation was therefore performed to investigate the density of the electron state of the atoms at the $NiSe_2$-(100)/$Ni(OH)_2$-(110) interface. The model build for the calculation is shown in Fig. 2c, and the partial density of states (PDOS) for each atom was calculated, as shown in Figs. 2f, g and S3. At the interface, the Ni atoms present typical conductive feature due to no

 https://doi.org/10.1007/s40820-020-0392-8

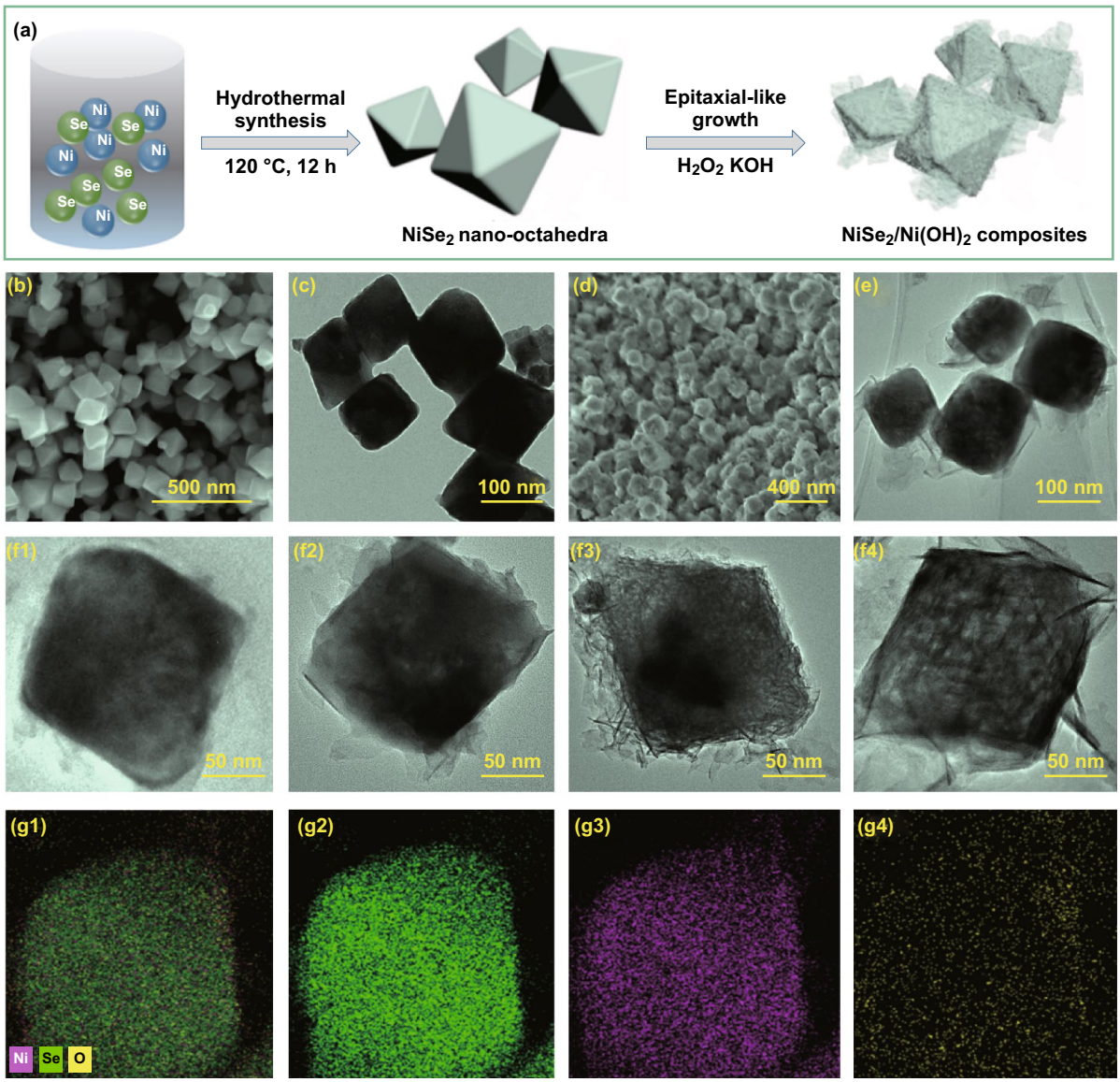

Fig. 1 **a** Synthetic process of $NiSe_2/Ni(OH)_2$ heterojunction composites. **b**, **c** SEM and TEM images of $NiSe_2$. **d**, **e** SEM and TEM images of $NiSe_2/Ni(OH)_2$-2h. **f**(1–4) TEM images of $NiSe_2/Ni(OH)_2$-1h, $NiSe_2/Ni(OH)_2$-2h, $NiSe_2/Ni(OH)_2$-3h, $NiSe_2/Ni(OH)_2$-6h. **g**(1–4) EDS mapping images of $NiSe_2/Ni(OH)_2$-2h

forbidden gap in their PDOSs, and furthermore, the PDOSs of Ni and O atoms in $Ni(OH)_2$ layers all present no forbidden gap, indicating the good electron conductivity at the interface, as well as a few layers of $Ni(OH)_2$ out of the interface. However, it is obvious that the forbidden gap tends to open in the PDOSs of Ni and O when $Ni(OH)_2$ layers are away from the interface. In layer 5, Ni and O atoms exhibit similar PDOSs compared with $Ni(OH)_2$. The PDOSs of Ni and Se atoms within the $NiSe_2$ layers close to the interface were also calculated, and they all present conductive feature with no forbidden gaps appear; as shown in Fig. S3, indicating the formation of $NiSe_2/Ni(OH)_2$ heterojunction does not influence the conductivity of $NiSe_2$. The DFT calculations well demonstrate the superiority of the $NiSe_2/Ni(OH)_2$ heterojunction for electron transport.

The XRD patterns of $NiSe_2$ and $NiSe_2/Ni(OH)_2$ heterojunction composites at different reaction time are presented in Fig. 3a. It is clear that all prepared samples exhibit strong $NiSe_2$ peaks, and $Ni(OH)_2$ peaks gradually increase with reaction time. The characteristic diffraction peaks at 29.80°, 33.41°, 36.70°, and 50.48° represent the (200), (210), (211), and (311) planes of $NiSe_2$, respectively. After treated in

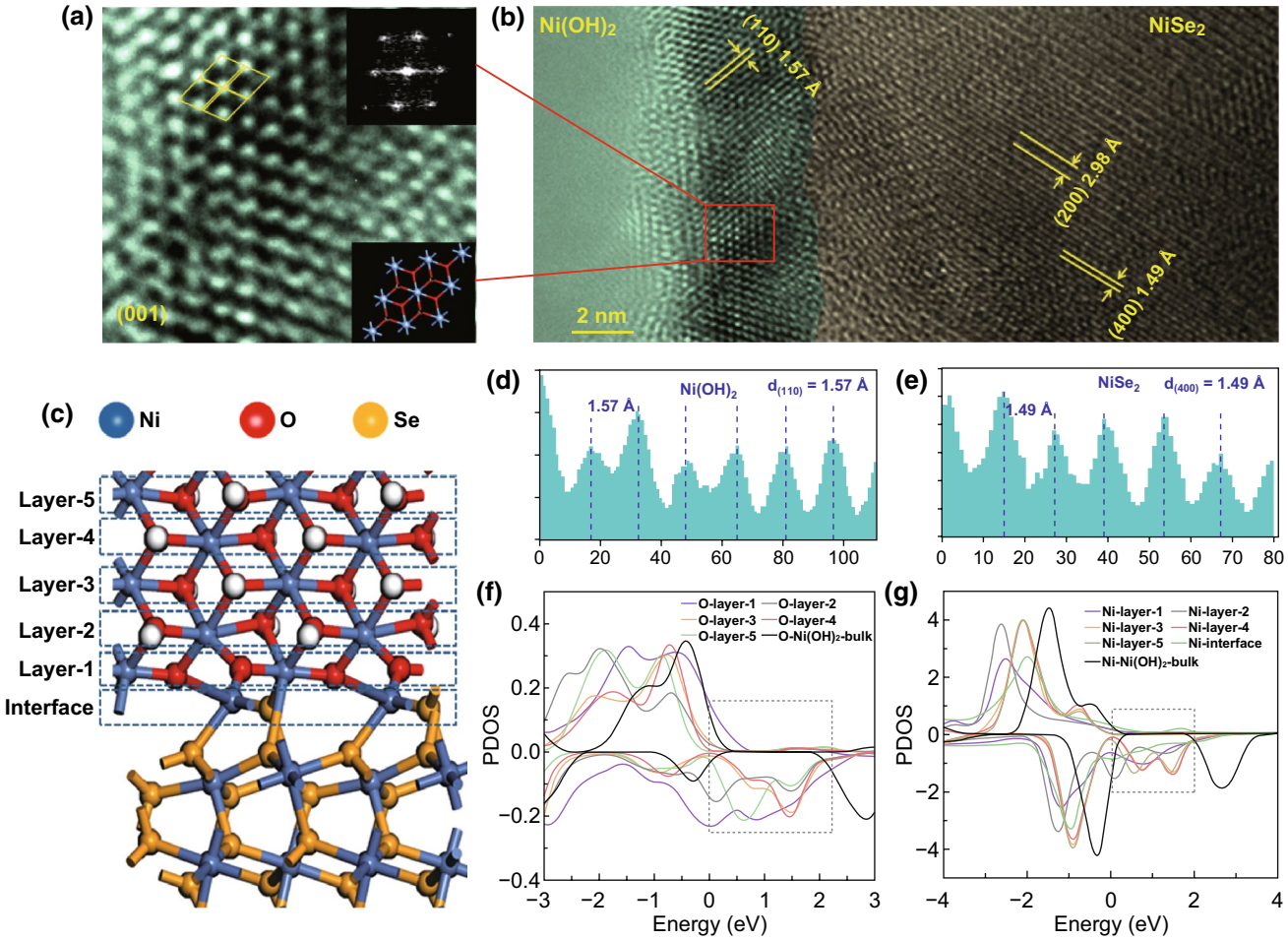

Fig. 2 **a**, **b** HRTEM images of $NiSe_2/Ni(OH)_2$ heterojunction. **c** The constructed $NiSe_2/Ni(OH)_2$ model for calculations. **d**, **e** Profile plots of the calibration for measuring the spacing in panels. **f**, **g** PDOS of O and Ni atoms at different layers

hydrogen peroxide and potassium hydroxide aqueous solution, the characteristic diffraction peaks of $Ni(OH)_2$ appear. Interestingly, $Ni(OH)_2$ peaks arose firstly at 2θ value of 59.05°, associated with the (110) planes of $Ni(OH)_2$. While the diffraction peaks at 19.26° and 38.54° belong to (001) and (101) planes, which are stronger than other peaks in the PDF standard card and for most reported $Ni(OH)_2$ nanomaterials, appear later than the (110) peak [44]. We suggest that the abnormally prior-growth of (110) peak is associated with the epitaxial-like crystallization of $Ni(OH)_2$ on the (110) plane.

XPS spectra were further collected to get insight into the surface chemical state changes during the treatments, as shown in Figs. 3b, c and S5. For the $NiSe_2$ precursor, the characteristic peaks of 853.52 and 870.94 eV are indexed to Ni $2p_{3/2}$ and Ni $2p_{1/2}$ due to the Ni–Se bond, and there is only negligible Ni–O peaks due to the trace NiO_x on the $NiSe_2$ surfaces [45]. After immersing into the KOH/H_2O_2 aqueous solution for 2 h, a noticeable change in the surface chemical state can be observed as demonstrated in the $NiSe_2/Ni(OH)_2$-2h XPS spectrum. The characteristic peaks at 856.04 and 873.93 eV are assigned to Ni $2p_{3/2}$ and Ni $2p_{1/2}$ due to Ni–O bond, indicting the formation of external $Ni(OH)_2$. Meanwhile, the Se 3d peak almost disappear in the $NiSe_2/Ni(OH)_2$-2h XPS spectrum while is strong in the $NiSe_2$ spectrum (Fig. 3c), implying the outer $NiSe_2$ has converted to $Ni(OH)_2$. It is worth mentioning that inner part of the $NiSe_2$ octahedra maintains since the XRD pattern of $NiSe_2/Ni(OH)_2$-2h still presents strong $NiSe_2$ characteristic peaks.

Based on the XRD and XPS results, we suggest the two steps of epitaxial process from $NiSe_2$ to $NiSe_2/Ni(OH)_2$ composites: initially, Se^- ion is oxidized by hydrogen peroxide, and Ni^{2+} ions are released into solutions. Subsequently, unreleased Ni atoms at the surfaces are coordinated to OH^- ions

https://doi.org/10.1007/s40820-020-0392-8

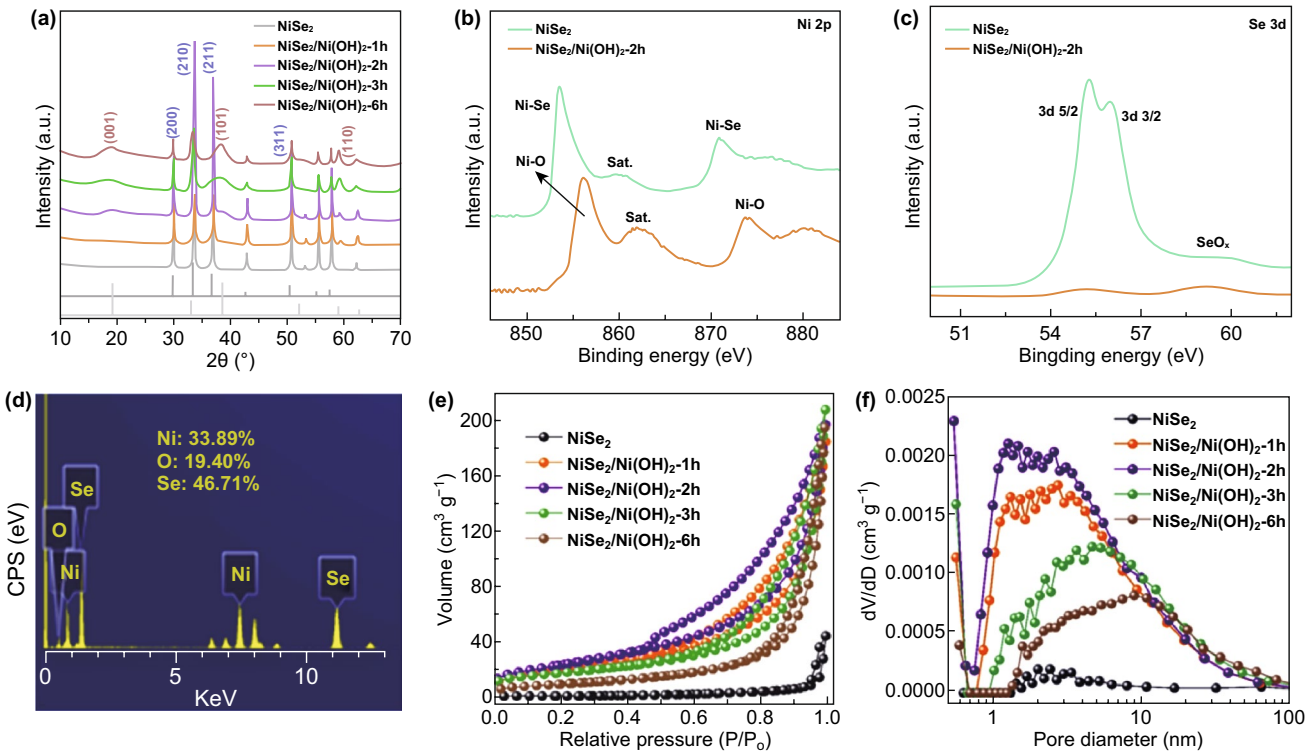

Fig. 3 **a** XRD pattern of $NiSe_2$ and $NiSe_2/Ni(OH)_2$ composite with different reaction times. **b** Ni 2p of $NiSe_2$ and $NiSe_2/Ni(OH)_2$-2h. **c** Se 2p of $NiSe_2$ and $NiSe_2/Ni(OH)_2$-2h. **d** EDX spectrum of $NiSe_2/Ni(OH)_2$-2h. **e** N_2 adsorption/desorption curves. **f** Pore size distribution curves

forming into a thin layer $Ni(OH)_2$ with (110) planes due to the restriction of $NiSe_2$ (100) planes. Meanwhile, the Ni^{2+} and OH^- ions in solution also precipitate on the $Ni(OH)_2$ (110) plane, contributing to the epitaxial-like route and the growth of (110) peak in the XRD pattern. Eventually, the $NiSe_2/Ni(OH)_2$ composites with $NiSe_2$-(100)/$Ni(OH)_2$-(110) heterojunction are achieved.

For better understanding the conversion process from $NiSe_2$ nano-octahedra to $NiSe_2/Ni(OH)_2$ heterojunction composites, we obtained the products from either pure hydrogen peroxide aqueous solution or pure potassium hydroxide aqueous solution. As illustrated in Fig. S4a, $NiSe_2$ in neither pure H_2O_2 solution nor pure KOH solution can be transformed to the desired $NiSe_2/Ni(OH)_2$ compositions. In the absence of H_2O_2, $NiSe_2$ retained the original phase without any change. Without KOH, the product is in multi-phase, and no $Ni(OH)_2$ peaks can be observed. Furthermore, we also immersed NiO into the KOH/H_2O_2 aqueous solution to demonstrate that the $Ni(OH)_2$ is originated from $NiSe_2$ rather than the trace NiO on the $NiSe_2$ surfaces. As shown in Fig. S4b, NiO maintains unchanged during the treatments. Therefore, we can conclude that immersing $NiSe_2$ in the KOH/H_2O_2 aqueous solution results in the epitaxial-like growth of $NiSe_2/Ni(OH)_2$ heterojunction composites.

Quantitatively analysis in the amounts of $NiSe_2$ and $Ni(OH)_2$ within the $NiSe_2/Ni(OH)_2$ is based on the EDX and TGA measurements. The EDX spectrum of $NiSe_2/Ni(OH)_2$-2h is displayed in Fig. 3d. The atom ratio of Ni, O, Se is 33.89%, 19.40%, 46.71%, respectively, and the molar ratio between $NiSe_2$ and $Ni(OH)_2$ is 2.4:1. However, due to that the EDX only focuses on a small spot, and it is irrational to conclude that the molar ratio within the whole sample is the same. Therefore, TGA tests were further employed to quantitatively investigate the compositional features of all $NiSe_2/Ni(OH)_2$ composites. As shown in Fig. S6 and Table S1, it is clearly that the mass fraction of $Ni(OH)_2$ increased with the reaction time, and the molar ratio between $NiSe_2$ and $Ni(OH)_2$ within $NiSe_2/Ni(OH)_2$-2h is 1.7:1, which is close than the value from EDX. At 6 h, most of the $NiSe_2$ has transformed to $Ni(OH)_2$, and the molar ratio between $NiSe_2$ and $Ni(OH)_2$ is 0.387:1, associated with the TEM results shown in Fig. 1f4. The TGA results clearly demonstrate that the growth of $Ni(OH)_2$ on $NiSe_2$ can be easy regulated depending on the treatment time.

Figure 3e displays the N_2 adsorption/desorption curves of the prepared samples. Obviously, $NiSe_2$ nano-octahedra show an extremely low N_2 adsorption capacity even at 1.0 P/P_0, implying its low specific surface associated with the well crystallized phase. However, after a controllable epitaxial-like growth, the obtained $NiSe_2/Ni(OH)_2$ composites exhibit much higher N_2 adsorption, indicating their enlarged specific surface areas. The calculated specific surface areas based on the N_2 adsorption/desorption isotherms of $NiSe_2$, $NiSe_2/Ni(OH)_2$-1h, $NiSe_2/Ni(OH)_2$-2h, $NiSe_2/Ni(OH)_2$-3h and $NiSe_2/Ni(OH)_2$-6h are 4.29, 73.59, 88.17, 63.59, and 36.29 $m^2\ g^{-1}$, respectively. Interestingly, $NiSe_2/Ni(OH)_2$-2h performs the largest surface areas, implying an non-proportional relation between reaction time and the porosity. The corresponding pore size distribution of prepared samples is displayed in Fig. 3f. Illustrated by the curves of $NiSe_2$, $NiSe_2/Ni(OH)_2$-1h, and $NiSe_2/Ni(OH)_2$-2h, the pore volume increases regularly in a range of 1–3 nm at the initial 2 h. When the reaction time is above 3 h, the pore volume in the size from 1 to 5 nm drastically reduces. Considering in that the molar ratio of $NiSe_2$ and $Ni(OH)_2$ is 1.41:1 for 3 h and 0.39:1 for 6 h, and it is highly likely that the further crystallization of $Ni(OH)_2$ after 2 h blocks the smaller pores. Therefore, we suggest an optimized reaction time is necessary to achieve larger surface areas and proper pore structures for supercapacitor applications, and here, $NiSe_2/Ni(OH)_2$-2h is the most promising one compared with its counterparts.

3.2 Electrochemical Analysis

The unique structure of $NiSe_2/Ni(OH)_2$ composites implies its potential as supercapacitor electrode material. Thus, for investigating the supercapacitance performances of $NiSe_2/Ni(OH)_2$ composites, a series of electrochemical characterizations including cyclic voltammetry (CV), galvanostatic discharge–charge (GCD), and electrochemical impedance spectroscopy (EIS) were employed, and the results are shown in Figs. 4 and S7. The CV curves of $NiSe_2$ and all $NiSe_2/Ni(OH)_2$ composites are presented at a scan rate of 5 mV s^{-1}. We can observe a pair of strong redox peaks, especially, $NiSe_2/Ni(OH)_2$-2h exhibits the strongest redox peaks, and the good symmetry of its redox peaks indicates the high Coulomb efficiency. The related electrochemical reactions were as follow (Eqs. 1 and 2) [46]:

$$NiSe_2 + OH^- \leftrightarrow NiSe_2OH + e^- \quad (1)$$

$$Ni(OH)_2 + OH^- \leftrightarrow NiOOH + H_2O + e^- \quad (2)$$

The specific capacities of all $NiSe_2/Ni(OH)_2$ electrode materials were calculated based on the GCD curves, and the results are presented in Fig. 4c. Corresponding to the CV curves, all GCD curves presented symmetric potential platforms resulted from reversible redox reactions (Fig. 4b). As expected, $NiSe_2/Ni(OH)_2$-2h shows much longer charge–discharge time, demonstrating its larger capacity than its counterparts. The specific capacity of $NiSe_2/Ni(OH)_2$-2h reaches a high value of 909 C g^{-1} (1818 F g^{-1}) at the current density of 1 A g^{-1}. Furthermore, at the current density of 20 A g^{-1}, the specific capacity of $NiSe_2/Ni(OH)_2$-2h is 597 C g^{-1} (1194 F g^{-1}), illustrating its good rate capability at large charge–discharge currents. Figure 4d shows the cycling tests of $NiSe_2$ and all $NiSe_2/Ni(OH)_2$ composites at the current density of 5 A/g. $NiSe_2$, $NiSe_2/Ni(OH)_2$-1h, $NiSe_2/Ni(OH)_2$-2h, $NiSe_2/Ni(OH)_2$-3h, and $NiSe_2/Ni(OH)_2$-6h present 89%, 84%, 85%, 69%, and 61% present capacity retention after 5000 cycles, respectively. Interestingly, $NiSe_2$, $NiSe_2/Ni(OH)_2$-1h, and $NiSe_2/Ni(OH)_2$-2h all present higher stability than other $NiSe_2/Ni(OH)_2$ composites synthesized with longer reaction time. Based on the TEM results in Fig. 1, we suggest longer reaction time that destroys the $NiSe_2$ octahedra foundation, leading to the unstable structures. Thus, it is concluded that the excellent stability is attributed to the high mechanical strength of $NiSe_2$ nano-octahedra. Furthermore, the electrochemical performance of $NiSe_2/Ni(OH)_2$-2h is competitive with other reported materials which is shown in Table S4, indicating tremendous potential as high-performance electrode materials.

I–V characteristic curves were examined, and the results are shown in Fig. 4e. It is apparent that $NiSe_2$ nano-octahedra and $NiSe_2/Ni(OH)_2$-2h exhibit preferable electron conductivity, much better than $Ni(OH)_2$. Especially, it is noteworthy that the $NiSe_2/Ni(OH)_2$-grind, which is prepared by simply mixing and grinding $NiSe_2$ and $Ni(OH)_2$ (the weight ratio of $Ni(OH)_2$ is 20%, same to the value in $NiSe_2/Ni(OH)_2$-2h) does not perform good conductivity. Therefore, it is concluded that the $NiSe_2/Ni(OH)_2$ heterojunction structure facilitate the electron transport, and the conductivity of $NiSe_2$ is well inherited in the $NiSe_2/Ni(OH)_2$ heterojunction composite.

https://doi.org/10.1007/s40820-020-0392-8

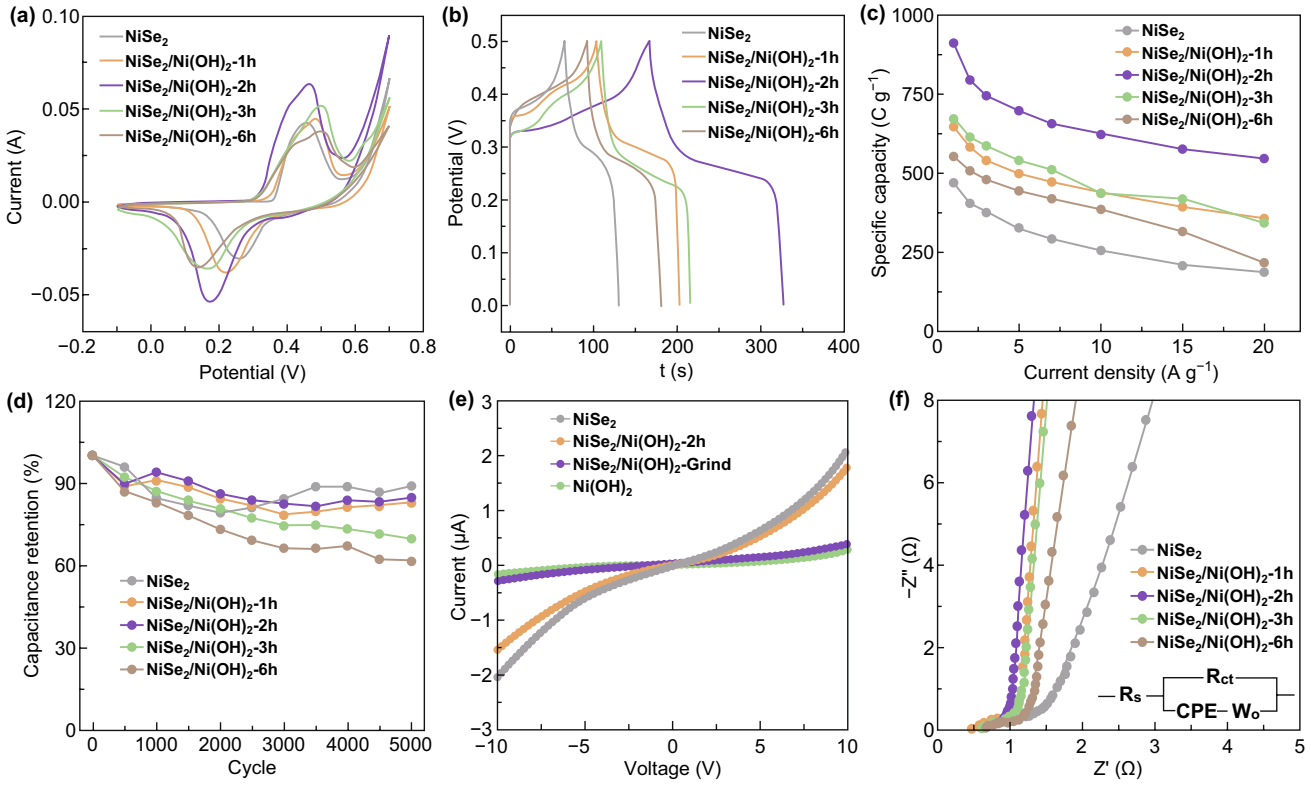

Fig. 4 **a** CV curves of prepared electrode at 5 mV s^{-1}. **b** GCD curves of prepared electrode at 5 A g^{-1}. **c** Comparison of specific capacity at different current density. **d** Cycling performance at 5 A g^{-1}. **e** I–V characterizations of prepared samples. **f** Nyquist plot of prepared electrode

Electrochemical impedance spectra were collected in a frequency range of 0.01–10^6 Hz and displayed in Fig. 4f. Obviously, the impedance spectra of all electrode materials perform similar curves, which composed of a semicircle in the high-frequency region and a sloping straight line in the low-frequency region. The impedance spectra of all electrodes were fitted using the equivalent circuit presented in the inset of Fig. 4f. R_s and R_{ct} are the electrolyte resistance and faradic resistance. On account of the depressed semicircle regions, CPE (constant phase angle element) was chosen rather than capacitor. Wo (Warburg element) was adopted to investigate the diffusion of electrolyte within the electrode. As listed in Table S2, the CPE-T values represent the EDLCs, and the CPE-P closing to 1 suggests the small leakage of current. It is apparent that $NiSe_2/Ni(OH)_2$-2h exhibit lower Rct of 0.222 Ω and Wo-R of 0.601 Ω compared with its counterparts, illustrating the rapid electrolyte diffusion and fast faradic reaction.

For better understanding the charge–discharge behavior of electrode materials, the scan rates and oxide peak current were fitted using Eq. 3 [21]:

$$i = av^b \tag{3}$$

The fitting results are presented in Fig. S8 and Table S3. Obviously, b-values of all the electrode materials are close to 0.5, indicating the diffusion-controlled behavior and battery-type charge–discharge process. It is worth mentioning that Eq. 3 is originated from Eq. 4 [21]:

$$i = i_{\mathrm{EDLC}} + i_{\mathrm{diff}} = k_1 v + k_2 v^{0.5} \tag{4}$$

In this formula, $k_1 v$ and $k_2 v^{0.5}$ are the capacitive contribution (i_{EDLC}) and diffusion contribution (i_{diff}) of current. The capacitive process including physical adsorption/desorption of electrolyte ions and fast surface redox reactions (capacitive contributions), and the diffusion process is kinetic sluggish redox reactions controlled by the diffusion of electrolyte ion (diffusion-controlled contributions). This method is suitable for batteries due to the narrow range of sweep rates and is widely used in many articles [47–49]. For supercapacitors, however, on account of the large range of sweep rate, this method is not appropriate. As shown in Fig. S9, the calculated areas originated from capacitive contribution ($k_1 v$)

exhibit strange shapes for all electrodes, of which the CVs are collected using the sweep rate from 5 to 25 mV/s. This can be explained by the theory mentioned in Ref. [46]. i_{EDLC} and i_{diff} can be expressed in details as Eqs. 5 and 6 [50]:

$$i_{diff} = k_1 v^{0.5} = nFA_{diff}C_0\left(D_0\right)^{0.5}(t)A_{diff}D_0^{0.5}, = nFv/RT \quad (5)$$

$$i_{EDLC} = k_2 v = A_{EDLC}C_d v A_{EDLC} \quad (6)$$

Herein, n and F are the electron number during the reaction (equal to 1 in our case) and faradic constant. A_{diff}, C_0, and D_0 are the electrochemical active surface area, reactant concentration, and diffusion efficiency of reactant, respectively. χ is a dimensionless number. A_{EDLC} and C_d are the electrochemical active area of EDLC and the specific capacitance of the double layer with the unit of F cm^{-2}, respectively. It is worth mentioning that χ is dependent to sweep rate v. Therefore, when the sweep rate range is narrow (the peak current does not drastically shift), it is reasonable to treat χ as a constant, and thus k_2 is also constant. However, in a wide sweep rate range (the peak current clearly shift with the sweep rate), treating χ as constant is not appropriate, and the equation of $i = k_1 v + k_2 v^{0.5}$ can only be applied to the peak current rather than the whole CVs [51]. Therefore, $k_1 v$ and $k_2 v^{0.5}$ are capacitive and diffusion contribution to the peak current, respectively.

Due to the aforementioned reasons, we used the equation of $i = k_1 v + k_2 v^{0.5}$ to fit the peak currents, and the fitting results are presented in Table 1 and Fig. S10. As shown in Table 1, the value of $k_1 v$ is much lower than $k_2 v^{0.5}$ in all electrode materials, demonstrating a distinct battery-type behavior. The capacitive contributions ($k_1 v$) for all electrodes are similar, while the diffusion contributions ($k_2 v^{0.5}$) are quite different. $NiSe_2$/$Ni(OH)_2$-2h performs a distinctly higher $k_2 v^{0.5}$ value of 0.15, larger than its counterparts, associated with its largest specific capacity, implying the largest amounts of electroactive sites. Considering in that the electroactive sites are mainly from $Ni(OH)_2$ and that $NiSe_2$/$Ni(OH)_2$-2h does not have the largest $Ni(OH)_2$ weight ratio, it is reasonable to conclude that the optimized $Ni(OH)_2$ amounts are necessary to guarantee the full utilization of the fast electron transportation in the heterojunction. Smaller amounts of $Ni(OH)_2$ cannot provide enough active sites. Overgrowth of $Ni(OH)_2$ leads to poor porosity and difficult transportation of electrons from active sites to the heterojunction. Both of them are detrimental to the specific capacity and rate performances.

We believe the enhancement of the battery-type $NiSe_2$/$Ni(OH)_2$ heterojunction electrode performances is mainly associated with the synergistic effects of this unique composite material. As is known, the fast ion migration and rapid electronic conductivity are essential for the performance of an electrode. The pure $NiSe_2$ nano-octahedra deliver a high electronic conductivity, but the low porosity cannot provide enough electrochemical active sites. After careful treatments, hierarchical porous $Ni(OH)_2$ shell forms on the outer surfaces of $NiSe_2$, providing abundant electrochemical active sites. Furthermore, the hierarchically porous structure provides rich pores for the ion migration (supported by the BET analysis), and the $NiSe_2$/$Ni(OH)_2$ heterojunction enabling the fast electron transportation at the interfaces (supported by the DFT calculations). Therefore, due to the formation of the $NiSe_2$/$Ni(OH)_2$ heterojunction, both the electron conductivity of the $NiSe_2$ and the fast ion migration in $Ni(OH)_2$ are fully utilized, enabling the remarkable performances of the $NiSe_2$/$Ni(OH)_2$ heterojunction electrode.

The contribution of $NiSe_2$ and $Ni(OH)_2$ is also analyzed, and the results are shown in Table S5. It is clearly seen that with the formation of $Ni(OH)_2$, the $NiSe_2$ contribution to the SC value decreases. We suggest it is due to the decreasing amounts of $NiSe_2$. The $Ni(OH)_2$ contribution reaches the maximum in $NiSe_2$/$Ni(OH)_2$-2h, although the $Ni(OH)_2$ fraction is larger in $NiSe_2$/$Ni(OH)_2$-3h and $NiSe_2$/$Ni(OH)_2$-6h associated with that the over crystallized $Ni(OH)_2$ does not present ideal pore structure, confirmed by the BET analyses.

Table 1 Fitted results of oxide peak current density versus scan rate ($v = 0.025$ V s^{-1})

	k_1	k_2	EDLC contributions $k_1 \times v$	Diffusion contributions $k_2 \times v^{0.5}$	Reduced Chi-square
$NiSe_2$	− 0.083	0.60	− 0.00208	0.0949	4.2 E^{-7}
$NiSe_2$/$Ni(OH)_2$-1h	0.35	0.64	0.00875	0.103	3.7 E^{-6}
$NiSe_2$/$Ni(OH)_2$-2h	0.27	0.95	0.00675	0.150	3.7 E^{-6}
$NiSe_2$/$Ni(OH)_2$-3h	0.21	0.74	0.00525	0.117	2.2 E^{-6}
$NiSe_2$/$Ni(OH)_2$-6h	0.25	0.50	0.00625	0.0791	1.8 E^{-6}

https://doi.org/10.1007/s40820-020-0392-8

The $NiSe_2/Ni(OH)_2$-2h presents the largest specific surface area of 88.17 $m^2\ g^{-1}$.

Therefore, we can conclude that the outstanding performance of $NiSe_2/Ni(OH)_2$-2h is attributed to the following reasons: First, the heterojunction between $Ni(OH)_2$ with high electrochemical activity and $NiSe_2$ with high conductivity improves the charge transportation within the electrode, enabling higher electrochemical activity. Meanwhile, the large specific surface area and abundant microscopes are preferable for the diffusion and transportation of electrolyte. Furthermore, the $NiSe_2$ octahedra foundation with high crystallinity is highly stable, enabling the long charge–discharge life.

3.3 Performances of the $NiSe_2/Ni(OH)_2$-2h//PPD-rGO Asymmetric Supercapacitor

The remarkable supercapacitance performance of $NiSe_2/Ni(OH)_2$-2h is due to the porous $Ni(OH)_2$ enabling the fast ion migration, the conductive and stable $NiSe_2$ octahedra ensuring the fast electron migration and cycling stability, as well as the $NiSe_2/Ni(OH)_2$ heterojunction offering an easy electron transportation from electroactive $Ni(OH)_2$ to conductive $NiSe_2$. For further investigating, the application of $NiSe_2/Ni(OH)_2$-2h for supercapacitors, a button asymmetric supercapacitor, was fabricated using 2.5 mg $NiSe_2/Ni(OH)_2$-2h as positive electrode and 4 mg PPD-rGO as negative electrode, as illustrated in Fig. 5a. The electrochemical performances of PPD-rGO are illustrated in Fig. S7f, l, and the FT-IR spectrum and the SEM image of PPD-rGO are presented in Fig. S11. The CV curves of PPD-rGO exhibit a typical double-layer capacitance behavior. Even at a high scan rate of 200 mV s^{-1}, it still remains a rectangle shape, indicating a fast charge transfer kinetics. The GCD curves of PPD-rGO from 1 to 50 A g^{-1} present a triangular shape and excellent symmetry, suggesting the highly reversible of charge–discharge process. Based on the GCDs, the specific capacity of PPD-rGO is calculated as 504 C g^{-1} (504 F g^{-1}), and a high value of 319 C g^{-1} (319 F g^{-1}) at 50 A g^{-1} indicates its excellent rate capability.

The electrochemical performances of $NiSe_2/Ni(OH)_2$-2h//PPD-rGO asymmetric supercapacitor are presented in Figs. 5b–f and S12. Calculated from the GCD curves of $NiSe_2/Ni(OH)_2$-2h//PPD-rGO, at a current density of 1 A g^{-1}, an ultrahigh specific capacity of 302 C g^{-1} (189 F g^{-1}) can be obtained. Furthermore, almost 100% coulomb efficiencies were acquired at different current densities (Fig. 5d). The energy density and power density can be acquired using Eqs. 7 and 8, and the results are shown in Fig. 5e [51]:

$$E = \frac{I}{m}\int_{t1}^{t2} V\mathrm{d}t \tag{7}$$

$$P = \frac{E}{\Delta t} \tag{8}$$

At the power density of 906.4 W kg^{-1}, the $NiSe_2/Ni(OH)_2$-2h//PPD-rGO is able to achieve the ultrahigh energy density of 76.1 Wh kg^{-1}. Moreover, the $NiSe_2/Ni(OH)_2$-2h//PPD-rGO exhibits a higher energy density and power density than many advanced asymmetric supercapacitors reported recently, such as NiCoP/NiCo-OH//AC [32], $NiSe_2$//AC [39], $NiCo_2O_4$//AC [52], $Ni(OH)_2$//AC [53], Cu_3SbS_4/Ni-5//Cu_2MoS_4/Ni [54], ZnNiCo-P//PPD-rGOs [27], CoNi-MOF//AC [55], $NiCoS_2$//AC [56], and Ag-rGO/$Ni(OH)_2$//AC [57] (Fig. 5e and Table S6). Take the advantage of high energy density and power density, these asymmetric supercapacitors can drive two electric fans for rotation. A red LED (1.6–3 V, 20 mA) 800 can also be lighted using the $NiSe_2/Ni(OH)_2$-2h//PPD-rGO asymmetric supercapacitor device. More importantly, the cycling stability test indicates this asymmetric device can have 82% retention of its original capacity after 8000 cycles. These tests strongly demonstrate the potential practical application of this asymmetric supercapacitor device.

4 Conclusions

In summary, using $NiSe_2$ nano-octahedra as the precursor, $NiSe_2/Ni(OH)_2$ heterojunction composites with large specific surface areas and rich micropores, as well as good electron conductivity, were successfully constructed through a epitaxial-like growth strategy. The porous $Ni(OH)_2$ enables the fast ion migration and large amount of electrochemical active sites, and the $NiSe_2$ nano-octahedra offer electron conductivity and mechanical strength for cycling stability. Noteworthy, the $NiSe_2/Ni(OH)_2$ heterojunction providing easy electron transportation from $Ni(OH)_2$ to $NiSe_2$, confirmed by the DFT calculations, is the domain reason contributing to the synergistic effects. Therefore, the $NiSe_2/$

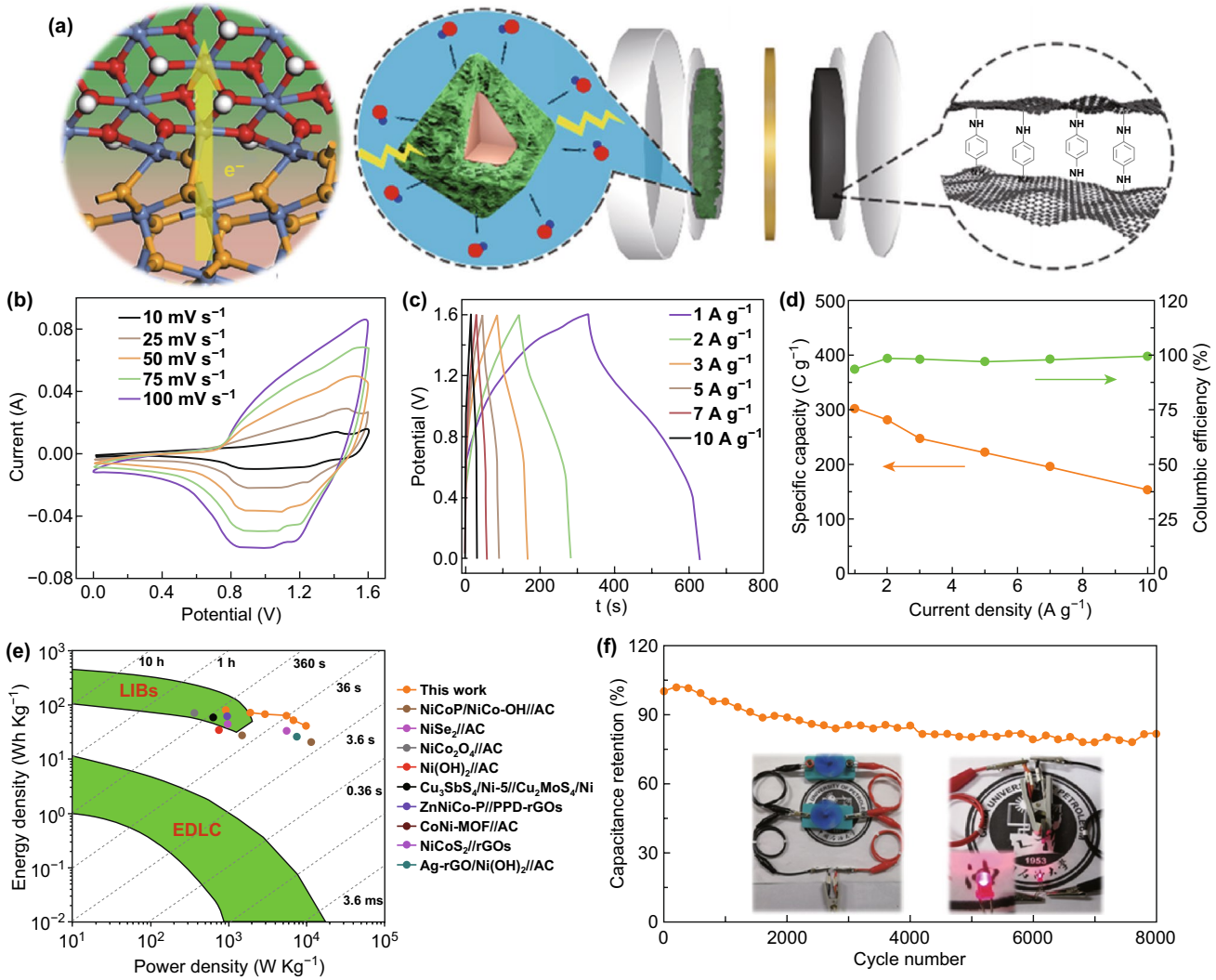

Fig. 5 **a** The assembled asymmetric supercapacitor, **b** CV curves, **c** GCD curves, **d** specific capacity and columbic efficiency at different current density, **e** Ragone plot, and **f** cycling performance

$Ni(OH)_2$ heterojunction composites obtained under optimized reaction conditions deliver a high specific capacity of 909 C g^{-1} at 1 A g^{-1}, an excellent cycling performance of 85% capacity retention after 5000 cycles. Furthermore, the fabricated $NiSe_2/Ni(OH)_2$//PPD-rGO button asymmetric supercapacitors achieve ultrahigh energy density of 76.1 Wh kg^{-1} at 906 W kg^{-1} and outstanding cycling stability of 82% capacity retention after 8000 cycles, indicating tremendous potential in practical application. Our work here provides a novel strategy to synthesize high-performance selenide/hydroxide composites. It needs more efforts to investigate if this method can be applied to other transition metal chalcogenide.

Acknowledgements This work was supported by the NSFC (Grant Nos. 21875285 and 21805155), Taishan Scholars Program (ts201511019), Key Research and Development Projects of Shandong Province (2019JZZY010331), and the Fundamental Research Funds for the Central Universities (19CX05001A).

Electronic supplementary material The online version of this article (https://doi.org/10.1007/s40820-020-0392-8) contains supplementary material, which is available to authorized users.

References

1. S. Chu, A. Majumdar, Opportunities and challenges for a sustainable energy future. Nature **488**, 294–303 (2012). https://doi.org/10.1038/nature11475
2. D.P. Dubal, N.R. Chodankar, D.H. Kim, P. Gomez-Romero, Towards flexible solid-state supercapacitors for smart and wearable electronics. Chem. Soc. Rev. **47**, 2065–2129 (2018). https://doi.org/10.1039/c7cs00505a
3. Y. Song, H. Chen, X. Chen, H. Wu, H. Guo, X. Cheng, B. Meng, H. Zhang, All-in-one piezoresistive-sensing patch integrated with micro-supercapacitor. Nano Energy **53**, 189–197 (2018). https://doi.org/10.1016/j.nanoen.2018.08.041
4. W. Guo, C. Yu, S. Li, Z. Wang, J. Yu, H. Huang, J. Qiu, Strategies and insights towards the intrinsic capacitive properties of MnO_2 for supercapacitors: challenges and perspectives. Nano Energy **57**, 459–472 (2019). https://doi.org/10.1016/j.nanoen.2018.12.015
5. Y. Cao, M. Li, J. Lu, J. Liu, K. Amine, Bridging the academic and industrial metrics for next-generation practical batteries. Nat. Nanotechnol. **14**, 200–207 (2019). https://doi.org/10.1038/s41565-019-0371-8
6. A. Konarov, N. Voronina, J.H. Jo, Z. Bakenov, Y. Sun, S. Myung, Present and future perspective on electrode materials for rechargeable zinc-ion batteries. ACS Energy Lett. **3**, 2620–2640 (2018). https://doi.org/10.1021/acsenergylett.8b01552
7. C. Yang, M. Sun, L. Zhang, P. Liu, P. Wang, H. Lu, $ZnFe_2O_4$@carbon core-shell nanoparticles encapsulated in reduced graphene oxide for high-performance Li-ion hybrid supercapacitors. ACS Appl. Mater. Interfaces **11**, 14713–14721 (2019). https://doi.org/10.1021/acsami.8b20305
8. R. Wang, Y. Han, Z. Wang, J. Jiang, Y. Tong, X. Lu, Nickel@nickel oxide core-shell electrode with significantly boosted reactivity for ultrahigh-energy and stable aqueous Ni–Zn battery. Adv. Funct. Mater. **28**, 1802157 (2018). https://doi.org/10.1002/adfm.201802157
9. H. Banda, S. Périé, B. Daffos, P. Taberna, L. Dubois et al., Sparsely pillared graphene materials for high-performance supercapacitors: improving ion transport and storage capacity. ACS Nano **13**, 1443–1453 (2019). https://doi.org/10.1021/acsnano.8b07102
10. S. Zhu, L. Li, J. Liu, H. Wang, T. Wang et al., Structural directed growth of ultrathin parallel birnessite on β-MnO_2 for high-performance asymmetric supercapacitors. ACS Nano **12**, 1033–1042 (2018). https://doi.org/10.1021/acsnano.7b03431
11. M. Yao, X. Ji, T. Chou, S. Cheng, L. Yang et al., Simple and cost-effective approach to dramatically enhance the durability and capability of a layered δ-MnO_2 based electrode for pseudocapacitors: a practical electrochemical test and mechanistic revealing. ACS Appl. Energy Mater. **2**, 2743–2750 (2019). https://doi.org/10.1021/acsaem.9b00075
12. C. Feng, J. Zhang, Y. He, C. Zhong, W. Hu, L. Liu, Y. Deng, Sub-3 nm Co_3O_4 nanofilms with enhanced supercapacitor properties. ACS Nano **9**, 1730–1739 (2015). https://doi.org/10.1021/nn506548d
13. V.D. Nithya, N.S. Arul, Review on α-Fe_2O_3 based negative electrode for high performance supercapacitors. J. Power Sources **327**, 297–318 (2016). https://doi.org/10.1016/j.jpowsour.2016.07.033
14. P. Sivakumar, M. Jana, M.G. Jung, A. Gedanken, H.S. Park, Hexagonal plate-like Ni–Co–Mn hydroxide nanostructures to achieve high energy density of hybrid supercapacitors. J. Mater. Chem. A **7**, 11362–11369 (2019). https://doi.org/10.1039/C9TA02583A
15. B. Zhao, D. Chen, X. Xiong, B. Song, R. Hu et al., A high-energy, long cycle-life hybrid supercapacitor based on graphene composite electrodes. Energy Storage Mater. **7**, 32–39 (2017). https://doi.org/10.1016/j.ensm.2016.11.010
16. P. Ge, S. Li, H. Shuai, W. Xu, Y. Tian et al., Engineering 1D chain-like architecture with conducting polymer towards ultra-fast and high-capacity energy storage by reinforced pseudo-capacitance. Nano Energy **54**, 26–38 (2018). https://doi.org/10.1016/j.nanoen.2018.09.062
17. G. Wang, L. Zhang, J. Zhang, A review of electrode materials for electrochemical supercapacitors. Chem. Soc. Rev. **41**, 797–828 (2012). https://doi.org/10.1039/c1cs15060j
18. Y. Shao, M.F. El-Kady, J. Sun, Y. Li, Q. Zhang et al., Design and mechanisms of asymmetric supercapacitors. Chem. Rev. **118**, 9233–9280 (2018). https://doi.org/10.1021/acs.chemrev.8b00252
19. X. Wu, L. Meng, Q. Wang, W. Zhang, Y. Wang, Wide potential window and high capacitance for flexible asymmetric supercapacitor based on Cu_2Se nanobrush and hydrangea-like $NiCo_2O_4$ microspheres. Chem. Eng. J. **354**, 346–350 (2018). https://doi.org/10.1016/j.cej.2018.08.045
20. R. Sahoo, D.T. Pham, T.H. Lee, T.H.T. Luu, J. Seok, Y.H. Lee, Redox-driven route for widening voltage window in asymmetric supercapacitor. ACS Nano **12**, 8494–8505 (2018). https://doi.org/10.1021/acsnano.8b04040
21. Y. Wang, Y. Song, Y. Xia, Electrochemical capacitors: mechanism, materials, systems, characterization and applications. Chem. Soc. Rev. **45**, 5925–5950 (2016). https://doi.org/10.1039/c5cs00580a
22. G. Nagaraju, S.C. Sekhar, B. Ramulu, J.S. Yu, An integrated approach toward renewable energy storage using rechargeable Ag@$Ni_{0.67}Co_{0.33}S$-based hybrid supercapacitors. Small **15**, 1805418 (2019). https://doi.org/10.1002/smll.201805418

23. F. Liu, L. Zeng, Y. Chen, R. Zhang, R. Yang et al., Ni-Co-N hybrid porous nanosheets on graphene paper for flexible and editable asymmetric all-solid-state supercapacitors. Nano Energy **61**, 18–26 (2019). https://doi.org/10.1016/j.nanoen.2019.04.003
24. Y. Huang, Y. Zeng, M. Yu, P. Liu, Y. Tong, F. Cheng, X. Lu, Recent smart methods for achieving high-energy asymmetric supercapacitors. Small Methods **2**, 1700230 (2018). https://doi.org/10.1002/smtd.201700230
25. Y. Guo, X. Hong, Y. Wang, Q. Li, J. Meng et al., Multicomponent hierarchical Cu-doped NiCo-LDH/CuO double arrays for ultralong-life hybrid fiber supercapacitor. Adv. Funct. Mater. (2019). https://doi.org/10.1002/adfm.201809004
26. R.R. Salunkhe, B.P. Bastakoti, C.T. Hsu, N. Suzuki, J.H. Kim, S.X. Dou, C.C. Hu, Y. Yamauchi, Direct growth of cobalt hydroxide rods on nickel foam and its application for energy storage. Chem. Eur. J. **20**(11), 3084–3088 (2014). https://doi.org/10.1002/chem.201303652
27. J. Li, Z. Liu, Q. Zhang, Y. Cheng, B. Zhao et al., Anion and cation substitution in transition-metal oxides nanosheets for high-performance hybrid supercapacitors. Nano Energy **57**, 22–33 (2019). https://doi.org/10.1016/j.nanoen.2018.12.011
28. X. Shi, J. Key, S. Ji, V. Linkov, F. Liu, H. Wang, H. Gai, R. Wang, Ni(OH)$_2$ nanoflakes supported on 3D Ni_3Se_2 nanowire array as highly efficient electrodes for asymmetric supercapacitor and Ni/MH battery. Small (2018). https://doi.org/10.1002/smll.201802861
29. C. Young, R.R. Salunkhe, J. Tang, C. Hu, M. Shahabuddin et al., Zeolitic imidazolate framework (ZIF-8) derived nanoporous carbon: the effect of carbonization temperature on the supercapacitor performance in an aqueous electrolyte. Phys. Chem. Chem. Phys. **18**(42), 29308–29315 (2016). https://doi.org/10.1039/C6CP05555A
30. Q. Zhou, T. Fan, Y. Li, D. Chen, S. Liu, X. Li, Hollow-structure NiCo hydroxide/carbon nanotube composite for High-Performance supercapacitors. J. Power Sources **426**, 111–115 (2019). https://doi.org/10.1016/j.jpowsour.2019.04.035
31. B. Dong, W. Li, X. Huang, Z. Ali, T. Zhang, Z. Yang, Y. Hou, Fabrication of hierarchical hollow Mn doped Ni(OH)$_2$ nanostructures with enhanced catalytic activity towards electrochemical oxidation of methanol. Nano Energy **55**, 37–41 (2019). https://doi.org/10.1016/j.nanoen.2018.10.050
32. X. Li, H. Wu, A.M. Elshahawy, L. Wang, S.J. Pennycook, C. Guan, J. Wang, Cactus-like NiCoP/NiCo-OH 3D architecture with tunable composition for high-performance electrochemical capacitors. Adv. Funct. Mater. **28**, 1800036 (2018). https://doi.org/10.1002/adfm.201800036
33. B. Kirubasankar, P. Palanisamy, S. Arunachalam, V. Murugadoss, S. Angaiah, 2D $MoSe_2$-Ni(OH)$_2$ nanohybrid as an efficient electrode material with high rate capability for asymmetric supercapacitor applications. Chem. Eng. J. **355**, 881–890 (2019). https://doi.org/10.1016/j.cej.2018.08.185
34. S. Min, C. Zhao, Z. Zhang, G. Chen, X. Qian, Z. Guo, Synthesis of Ni(OH)$_2$/rGO pseudocomposite on nickel foam for supercapacitors with superior performance. J. Mater. Chem. A **3**, 3641–3650 (2015). https://doi.org/10.1039/C5TA06174A
35. J. Ji, L.L. Zhang, H. Ji, Y. Li, X. Zhao et al., Nanoporous Ni(OH)$_2$ thin film on 3D ultrathin-graphite foam for asymmetric supercapacitor. ACS Nano **7**, 6237–6243 (2013). https://doi.org/10.1021/nn4021955
36. J. Yan, Z. Fan, W. Sun, G. Ning, T. Wei et al., Advanced asymmetric supercapacitors based on Ni(OH)$_2$/graphene and porous graphene electrodes with high energy density. Adv. Funct. Mater. **22**, 2632–2641 (2012). https://doi.org/10.1002/adfm.201102839
37. W. Wei, J. Wu, S. Cui, Y. Zhao, W. Chen, L. Mi, α-Ni(OH)$_2$/$NiS_{1.97}$ heterojunction composites with excellent ion and electron transport properties for advanced supercapacitors. Nanoscale **11**, 6243–6253 (2019). https://doi.org/10.1039/C9NR00962K
38. Z. Ma, F. Jing, Y. Fan, L. Hou, L. Su, L. Fan, G. Shao, High-stability MnO_x nanowires@C@MnO_x nanosheet core-shell heterostructure pseudocapacitance electrode based on reversible phase transition mechanism. Small (2019). https://doi.org/10.1002/smll.201900862
39. S. Wang, W. Li, L. Xin, M. Wu, Y. Long, H. Huang, X. Lou, Facile synthesis of truncated cube-like $NiSe_2$ single crystals for high-performance asymmetric supercapacitors. Chem. Eng. J. **330**, 1334–1341 (2017). https://doi.org/10.1016/j.cej.2017.08.078
40. X. Lu, L. Li, B. Song, K. Moon, N. Hu, G. Liao, T. Shi, C. Wong, Mechanistic investigation of the graphene functionalization using p-phenylenediamine and its application for supercapacitors. Nano Energy **17**, 160–170 (2015). https://doi.org/10.1016/j.nanoen.2015.08.011
41. B. Xu, K.M. Poduska, Linking crystal structure with temperature-sensitive vibrational modes in calcium carbonate minerals. Phys. Chem. Chem. Phys. **16**, 17634–17639 (2014). https://doi.org/10.1039/C4CP01772B
42. S. Gadipelli, W. Travis, W. Zhou, Z. Guo, A thermally derived and optimized structure from ZIF-8 with giant enhancement in CO_2 uptake. Energy Environ. Sci. **7**, 2232–2238 (2014). https://doi.org/10.1039/C4EE01009D
43. H.T. Kwon, H. Jeong, A.S. Lee, H.S. An, J.S. Lee, Heteroepitaxially grown zeolitic imidazolate framework membranes with unprecedented propylene/propane separation performances. J. Am. Chem. Soc. **137**, 12304–12311 (2015). https://doi.org/10.1021/jacs.5b06730
44. T. Wang, G. Nam, Y. Jin, X. Wang, P. Ren et al., NiFe (Oxy) hydroxides derived from nife disulfides as an efficient oxygen evolution catalyst for rechargeable Zn-air batteries: the effect of surface S residues. Adv. Mater. **30**, 1800757 (2018). https://doi.org/10.1002/adma.201800757
45. X. Xu, F. Song, X. Hu, A nickel iron diselenide-derived efficient oxygen-evolution catalyst. Nat. Commun. **7**, 12324 (2016). https://doi.org/10.1038/ncomms12324
46. X. Li, H. Wu, C. Guan, A.M. Elshahawy, Y. Dong, S.J. Pennycook, J. Wang, (Ni, Co)Se_2/NiCo-LDH core/shell structural electrode with the cactus-like (Ni, Co)Se_2 core for asymmetric supercapacitors. Small (2018). https://doi.org/10.1002/smll.201803895

 https://doi.org/10.1007/s40820-020-0392-8

47. D. Cao, W. Kang, S. Wang, Y. Wang, K. Sun et al., In situ N-doped carbon modified $(Co_{0.5}Ni_{0.5})_9S_8$ solid-solution hollow spheres as high-capacity anodes for sodium-ion batteries. J. Mater. Chem. A **7**, 8268–8276 (2019). https://doi.org/10.1039/C9TA00709A
48. H. Wu, Q. Yu, C. Lao, M. Qin, W.A. Wang et al., Scalable synthesis of VN quantum dots encapsulated in ultralarge pillared N-doped mesoporous carbon microsheets for superior potassium storage. Energy Storage Mater. **18**, 43–50 (2019). https://doi.org/10.1016/j.ensm.2018.09.025
49. T. Yang, Y. Liu, D. Yang, B. Deng, Z. Huang et al., Bimetallic metal-organic frameworks derived Ni–Co–Se@C hierarchical bundle-like nanostructures with high-rate pseudocapacitive lithium ion storage. Energy Storage Mater. **17**, 374–384 (2019). https://doi.org/10.1016/j.ensm.2018.05.024
50. A.J. Bard, L.R. Faulkner, *Electrochemical methods: fundamentals and applications*, 2nd edn. (Wiley, New yolk, 2001), pp. 45–86.
51. S. Zhang, Z. Yang, K. Gong, B. Xu, H. Mei et al., Temperature controlled diffusion of hydroxide ions in 1D channels of Ni-MOF-74 for its complete conformal hydrolysis to hierarchical $Ni(OH)_2$ supercapacitor electrodes. Nanoscale **11**, 9598–9607 (2019). https://doi.org/10.1039/C9NR02555C
52. Y. Xue, T. Chen, S. Song, P. Kim, J. Bae, DNA-directed fabrication of $NiCo_2O_4$ nanoparticles on carbon nanotubes as electrodes for high-performance battery-like electrochemical capacitive energy storage device. Nano Energy **56**, 751–758 (2019). https://doi.org/10.1016/j.nanoen.2018.11.003
53. W. He, G. Zhao, P. Sun, P. Hou, L. Zhu et al., Construction of Longan-like hybrid structures by anchoring nickel hydroxide on yolk-shell polypyrrole for asymmetric supercapacitors. Nano Energy **56**, 207–215 (2019). https://doi.org/10.1016/j.nanoen.2018.11.048
54. V.K. Mariappan, K. Krishnamoorthy, P. Pazhamalai, S. Sahoo, S.S. Nardekar, S. Kim, Nanostructured ternary metal chalcogenide-based binder-free electrodes for high energy density asymmetric supercapacitors. Nano Energy **57**, 307–316 (2019). https://doi.org/10.1016/j.nanoen.2018.12.031
55. T. Deng, Y. Lu, W. Zhang, M. Sui, X. Shi, D. Wang, W. Zheng, Inverted design for high-performance supercapacitor via $Co(OH)_2$-derived highly oriented MOF electrodes. Adv. Energy Mater. **8**, 1702294 (2018). https://doi.org/10.1002/aenm.201702294
56. W. He, C. Wang, H. Li, X. Deng, X. Xu, T. Zhai, Ultrathin and porous $Ni_3S_2/CoNi_2S_4$ 3D-network structure for superhigh energy density asymmetric supercapacitors. Adv. Energy Mater. **7**, 1700983 (2017). https://doi.org/10.1002/aenm.201700983
57. E. Cho, C. Chang-Jian, K. Lee, J. Huang, B. Ho, R. Liu, Y. Hsiao, Ternary composite based on homogeneous $Ni(OH)_2$ on graphene with Ag nanoparticles as nanospacers for efficient supercapacitor. Chem. Eng. J. **334**, 2058–2067 (2018). https://doi.org/10.1016/j.cej.2017.11.175